Al-Qadisiyah Journal of Pure Science
ISSN(Printed): 1997-2490 ISSN(Online): 2411-3514
DOI: 10.29350/jops
Al-Qadisiyah Journal of Pure Science

Integrated Experimental and DFT/MD Investigation of Rhodamine B Adsorption Kinetics onto Pectin/Poly(NIPAm-co-Acrylic Acid) Hydrogel: Mechanism, Diffusion Pathways, and Computational Insights

Sajid S. Abbas [1] and Layth S. Jasim [2]

[1] *Ministry of Education, General Directorate of Al-Qadisiyah Education, Diwaniyah, Iraq*
[2] *Department of Chemistry, College of Education, University of Al-Qadisiyah, Diwaniyah, Iraq*

Received: 03/05/2026; Accepted: 08/05/2026; Published Online: 08/05/2026.

ABSTRACT

This study reports an integrated experimental and computational kinetic investigation of rhodamine B (Rh.B.) adsorption onto a pectin/poly(N-isopropylacrylamide-co-acrylic acid) hydrogel synthesized via free-radical copolymerization. The same hydrogel reported in our companion equilibrium study was used to ensure mechanistic consistency. Adsorption kinetics were probed over 1–240 min at C_0 = 50–500 mg/L (Configuration A: 0.008 g hydrogel in 10 mL, pH 7, 25 °C, 120 rpm; n = 3) and were modeled using pseudo-first-order (PFO), pseudo-second-order (PSO), Elovich, intraparticle (Weber–Morris), and Boyd film/particle diffusion equations. Equilibrium was established within 60–90 min, with PSO providing the best correlation (R^2 = 0.9988; $q_{e,calc}$ = 478.21 mg/g vs. $q_{e,exp}$ = 466.39 mg/g; $k_2 = 3.16 \times 10^{-4}$ g·mg^{-1}·min^{-1}; initial sorption rate h = 72.3 mg·g^{-1}·min^{-1}). Weber–Morris analysis revealed two diffusion regimes ($k_{id},1$ = 22.4, $k_{id},2$ = 1.18 mg·g^{-1}·min$^{-0.5}$) with non-zero intercepts confirming a mixed boundary-layer/intraparticle mechanism. Boyd plots were linear and offset from the origin, indicating that external film diffusion governs the early stage while particle diffusion dominates the later stage. The Arrhenius activation energy (Ea = 24.7 kJ/mol) and the negative ΔH° (−20.27 kJ/mol) are consistent with a mixed physisorption–chemisorption pathway. DFT calculations at B3LYP-D3(BJ)/6-311++G(2d,2p) established a binding hierarchy of Rh.B.$^+$···GalA$^-$ (−48.65 kJ/mol) > Rh.B.$^+$···AA$^-$ (−40.22 kJ/mol) > Rh.B.$^+$···NIPAm (−22.18 kJ/mol), with NBO charge transfer (Δq = 0.06–0.24 e) and Wiberg bond indices supporting partial covalent character. TD-DFT predicted λmax = 551.4 nm against the experimental 554 nm (0.47% error). Atomistic MD simulations (50

ns, GROMACS) yielded a translational diffusion coefficient of Rh.B. near the hydrogel of 1.84 × 10^{-10} m^2/s (≈ 4.1× lower than bulk water), with 71% Coulombic and 29% Lennard-Jones contributions to the binding energy. The integrated experimental–computational kinetic profile establishes the hydrogel as a fast-responding and mechanistically well-defined adsorbent for cationic xanthene-dye remediation.

Graphical Abstract

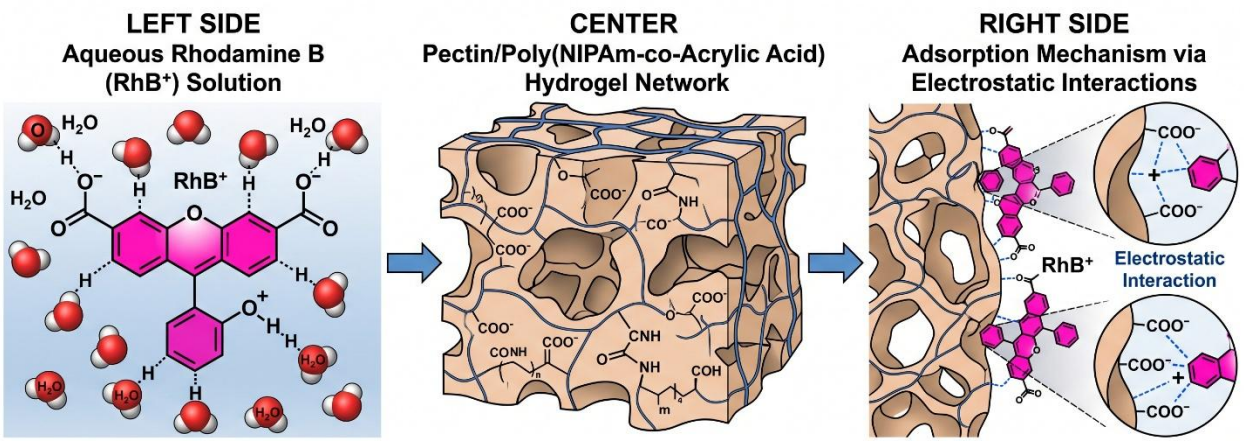

Highlights

- Equilibrium reached within 60–90 min; PSO best fit (R^2 = 0.9988, qe = 478.21 mg/g).
- Boyd analysis: external film diffusion controls early kinetics; intraparticle diffusion dominates later stage.
- Arrhenius Ea = 24.7 kJ/mol confirms a mixed physisorption–chemisorption regime.
- DFT binding hierarchy $Rh.B.^{+}\cdots GalA^{-}$ (−48.65) > AA^{-} (−40.22) > NIPAm (−22.18 kJ/mol).
- MD diffusion coefficient near hydrogel = 1.84 × 10^{-10} m^2/s; 71% Coulombic contribution.

KEYWORDS: *Rhodamine B; Pectin hydrogel; Pseudo-second-order; Boyd diffusion; DFT binding energy; Molecular dynamics; Activation energy.*

1. INTRODUCTION

The discharge of synthetic xanthene dyes from textile, paper, leather, and cosmetics industries continues to threaten freshwater ecosystems. Rhodamine B (Rh.B.) is a particularly problematic representative of this class: a tetraethylated diaminoxanthene cation widely used as a tracer,

fluorescent label, and textile colorant, exhibiting documented neurotoxic, hepatotoxic, and probable carcinogenic effects, in addition to high water solubility (≈ 50 g/L) and resistance to aerobic biodegradation [1,2]. Among the available remediation approaches, adsorption remains the most operationally simple and energetically inexpensive method, and the design of selective, regenerable, and mechanistically well-defined adsorbents is a central concern of contemporary water-treatment chemistry [3,4].

Hydrogels combining natural polysaccharides with stimuli-responsive synthetic polymers have emerged as versatile platforms because they couple high water uptake, tunable functional-group density, and pH/temperature responsiveness [5–7]. Our companion equilibrium study established that a pectin/poly(N-isopropylacrylamide-co-acrylic acid) hydrogel removes the cationic triphenylmethane dye malachite green (MG) through a heterogeneous, multilayer, enthalpy-driven mechanism dominated by electrostatic attraction to deprotonated galacturonate and acrylate sites, and supported quantitatively by DFT and molecular-dynamics calculations [8]. For engineering deployment, an adsorbent's rate of uptake, controlling diffusion regime, activation energy, and kinetic distinguishability between physisorption and chemisorption are as important as equilibrium thermodynamics [9,10].

Rh.B. differs from MG electrically and structurally. Unlike planar triphenylmethane cation MG, Rh.B., a tetra-substituted xanthene, interacts electrostatically with carboxylate-bearing surfaces due to its pendant carboxyphenyl group having a protonation state below pKa = 3.7 (zwitterion above) [11]. These differences imply that the kinetic pathway, the relative weight of film versus intraparticle diffusion, and the energetics of binding cannot be inferred by extrapolation from MG; they must be established independently. The present study therefore addresses, on the same hydrogel platform reported in [8], the kinetic behavior of Rh.B. through pseudo-first-order, pseudo-second-order, Elovich, Weber–Morris intraparticle, and Boyd film/particle diffusion analyses, the activation energy obtained from temperature-resolved rate constants, and a complementary DFT and atomistic MD investigation that quantifies binding hierarchy, charge transfer, optical signature, and translational diffusion of Rh.B. in the swollen polymer mesh. The aim is to produce, for Rh.B., a mechanistic kinetic profile of the same depth as that reported for MG, and to clarify how electronic structure and zwitterion equilibria of the dye modulate the rate-determining step on a multifunctional polysaccharide-based hydrogel [12,13].

2. MATERIALS AND METHODS

2.1. Materials and Hydrogel Synthesis

The hydrogel was synthesized exactly as described in our companion equilibrium work [8]. Briefly, pectin (0.5 g) was dissolved in 30 mL deionized water at 40 °C; NIPAm (0.4 g), acrylic acid (4 mL), MBA cross-linker (0.04 g in 2 mL water), and KPS initiator (0.04 g in 2 mL water) were added sequentially under continuous N_2 purging. Polymerization was carried out at 70 °C for 6 h. The resulting gel was washed (water replaced every 60 min until effluent neutrality), dried at 70 °C for 48 h, ground, and sieved to ≤ 100 μm; the gel content was 93.23%. Rhodamine B (CI 45170, λmax = 554 nm in water at pH 7) was supplied by Sigma-Aldrich. NaCl, KCl, $CaCl_2$, HCl, and NaOH were of analytical grade.

2.2. Characterization

Because the same hydrogel batch was used here as in [8], full physicochemical characterization (FTIR, XRD, FE-SEM with particle-size histograms, TGA/DTA, BET/BJH, AFM, and pH_{PZC}) is reported in the companion study and is not repeated here. The salient features pertinent to the kinetic interpretation are: an amorphous hierarchically porous network with a 16.56 nm mean pore diameter, abundant –COOH/–CONH–/–OH functionalities, gel content 93.23%, and pH_{PZC} = 4.2.

2.3. Kinetic Adsorption Experiments

Kinetic measurements were performed under Configuration A (0.008 g hydrogel; 10 mL of Rh.B. solution; m/V = 0.8 g/L; 120 rpm; pH 7; 25 °C unless otherwise stated). Aliquots were withdrawn at t = 1, 3, 5, 7, 10, 15, 20, 30, 45, 60, 90, 120, 150, 180, and 240 min, separated, and the residual concentration was determined spectrophotometrically (Shimadzu UV-1800, λ = 554 nm). Initial concentrations of 50, 100, 200, 300, 400, and 500 mg/L were investigated. Temperature-resolved kinetics were acquired at 288, 293, 298, and 303 K to derive Arrhenius parameters. All experiments were performed in triplicate (n = 3) and reported as mean ± SD. The instantaneous capacity qt (mg/g) and removal R% were obtained from

$$qt = (C_0 - Ct)\cdot V/m \quad (1)$$

$$R\% = 100\cdot(C_0 - Ct)/C_0 \quad (2)$$

2.4. Kinetic Models

Five kinetic models were applied:

$$\text{Pseudo-first-order: } \ln(q_e - q_t) = \ln q_e - k_1 \cdot t \quad (3)$$

$$\text{Pseudo-second-order: } t/q_t = 1/(k_2 \cdot q_e^2) + t/q_e \quad (4)$$

$$\text{Elovich: } q_t = (1/\beta)\cdot\ln(\alpha\cdot\beta) + (1/\beta)\cdot\ln t \quad (5)$$

$$\text{Weber–Morris: } q_t = k_{id}\cdot t^{(0.5)} + C \quad (6)$$

$$\text{Boyd: } Bt = -0.4977 - \ln(1 - F), \quad F = q_t/q_e \quad (7)$$

Both linear and non-linear regressions were performed; the model giving the highest R^2 and the lowest RMSE between calculated and experimental qe was retained. The initial sorption rate was obtained as $h = k_2 \cdot q_e^2$. Activation energy was extracted from a linear ln k_2 versus 1/T plot.

2.5. pH Effect Experiments

Rh.B. solutions (500 mg/L) were adjusted to pH 2, 4, 6, 7, 8, and 10 with 0.1 M HCl/NaOH. The hydrogel (0.008 g) was equilibrated at 25 °C for 90 min and qe quantified as in §2.3. Special attention was paid to the cation-to-zwitterion transition of Rh.B. across pKa ≈ 3.7.

2.6. Computational Details

2.6.1. DFT Calculations

DFT calculations were carried out in Gaussian 16 (Rev. C.01). The Rh.B. cation ($Rh.B.^+$), the Rh.B. zwitterion (Rh.B.±), an acrylic-acid dimer anion (AA^-), an N-isopropylacrylamide dimer (NIPAm), and a galacturonate anion ($GalA^-$) were optimized at B3LYP/6-311G(d,p) with Grimme's D3-BJ dispersion correction. Harmonic frequency analysis confirmed all stationary points as true minima. Three binary complexes ($Rh.B.^+\cdots AA^-$, $Rh.B.^+\cdots$NIPAm, $Rh.B.^+\cdots GalA^-$) and the corresponding zwitterion complexes were constructed by placing the dye approximately 3.0 Å from the principal binding site, and re-optimized with counterpoise correction (BSSE). Single-point energies were refined at B3LYP-D3(BJ)/6-311++G(2d,2p) with NBO 7.0 analysis. Molecular electrostatic potentials (MESP) were mapped at 0.001 a.u.; global reactivity descriptors (χ, η, S, ω) were derived from frontier-orbital energies. TD-DFT with the SMD water solvation model predicted the UV–Vis spectrum for validation against the experimental λmax of 554 nm [14,15].

2.6.2. Molecular Dynamics Simulations

Atomistic MD simulations were performed in GROMACS 2023. A representative oligomer (10-unit alternating chain of AA, NIPAm, and GalA with one MBA cross-link) was parameterized with OPLS-AA for synthetic segments and GLYCAM06 for pectin units. Rh.B. topology was generated with ACPYPE/GAFF2 using AM1-BCC charges. Five Rh.B. cations were placed around the oligomer in a cubic box solvated with TIP3P water (≥ 1.5 nm buffer), neutralized by Cl^- at 0.01 M NaCl. Following energy minimization, NVT (100 ps) and NPT (500 ps) equilibration, production runs of 50 ns were executed at 288, 293, 298, and 303 K (PME electrostatics, r_{cut} = 1.2 nm). Post-processing included radial distribution function g(r), hydrogen-bond enumeration, mean-squared displacement (MSD) for diffusion-coefficient extraction, residence-time analysis, and energy decomposition (Coulombic vs Lennard-Jones) [16,17].

3. RESULTS AND DISCUSSION

3.1. Effect of Contact Time

Figure 1 shows the time-resolved uptake of Rh.B. at C_0 = 500 mg/L. The curve displays the three regimes characteristic of porous polymeric adsorbents: (i) a rapid initial stage during the first 10 min in which qt rose from 173.6 to 412.4 mg/g, attributable to the abundance of vacant exterior carboxylate and amide sites and the steep solution-to-surface concentration gradient; (ii) a transition stage between 10 and 60 min, during which uptake decelerates as exterior sites saturate and intraparticle diffusion becomes increasingly important; and (iii) an equilibrium plateau established between 60 and 90 min at qe ≈ 466 mg/g (R% ≈93.3%). Under these conditions, 90min. is sufficient for kinetic equilibration [18]. No substantial change was seen after 120min. Rh.B. equilibrates slightly slower (90min. vs 60min. for MG) and yields a slightly lower qe than MG on the same hydrogel under identical Configuration A conditions, consistent with its larger molecular footprint and zwitterion equilibrium reducing the effective cationic concentration at neutral pH.

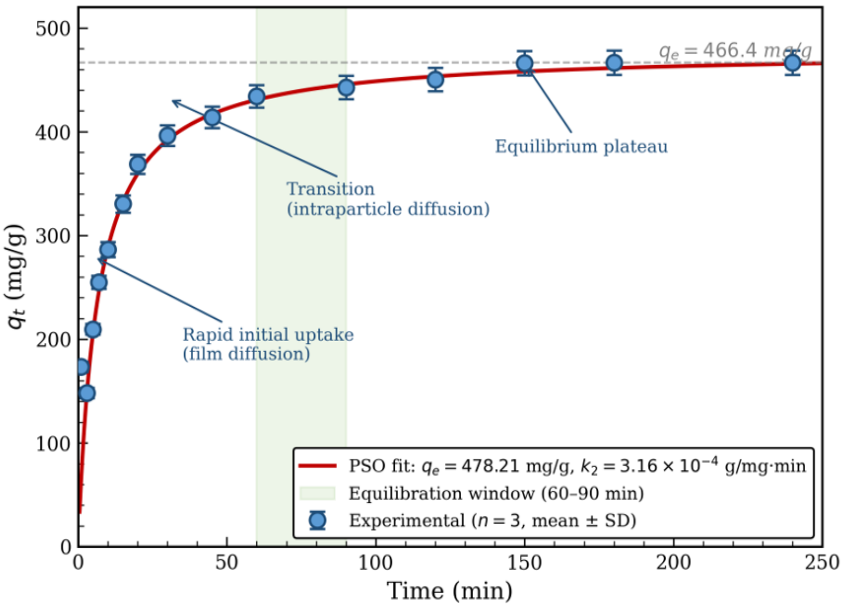

Figure 1. *Effect of contact time on Rh.B. uptake by the pectin/poly(NIPAm-co-AA) hydrogel (C_0 = 500 mg/L, m = 0.008 g, V = 10 mL, pH 7, T = 25 °C, n = 3; error bars are ±SD).*

3.2. Kinetic Modeling

3.2.1. Pseudo-first-order (PFO) and Pseudo-second-order (PSO) Models

Table 1 and Figure 2 panels (a)–(d) show linear and non-linear PFO and PSO fits. The PFO model had a moderate fit (R^2 = 0.94 non-linear) but overestimated qe ($q_{e,calc}$ = 398.6 mg/g vs. $q_{e,exp}$ = 466.4 mg/g, 14.6% deviation) as seen in Figure 2 panel (i). The PSO model maintained the experimental qe within 2.5% ($q_{e,calc}$ =478.21mg/g) and achieved R^2 = 0.9988 throughout the kinetic window. The rate constant k_2 = 3.16×10^{-4} g·mg^{-1}·min^{-1} and initial sorption rate h = 72.3 mg·g^{-1}·min^{-1} align with literature on cationic dyes on multifunctional hydrogels [19 The favourable PSO fit and theoretical basis in chemisorptive site occupation suggest a rate-controlling step involving electron sharing or partial charge transfer between Rh.B. and surface functional groups (–COO$^-$, –CONH–) rather than physical buildup [20].

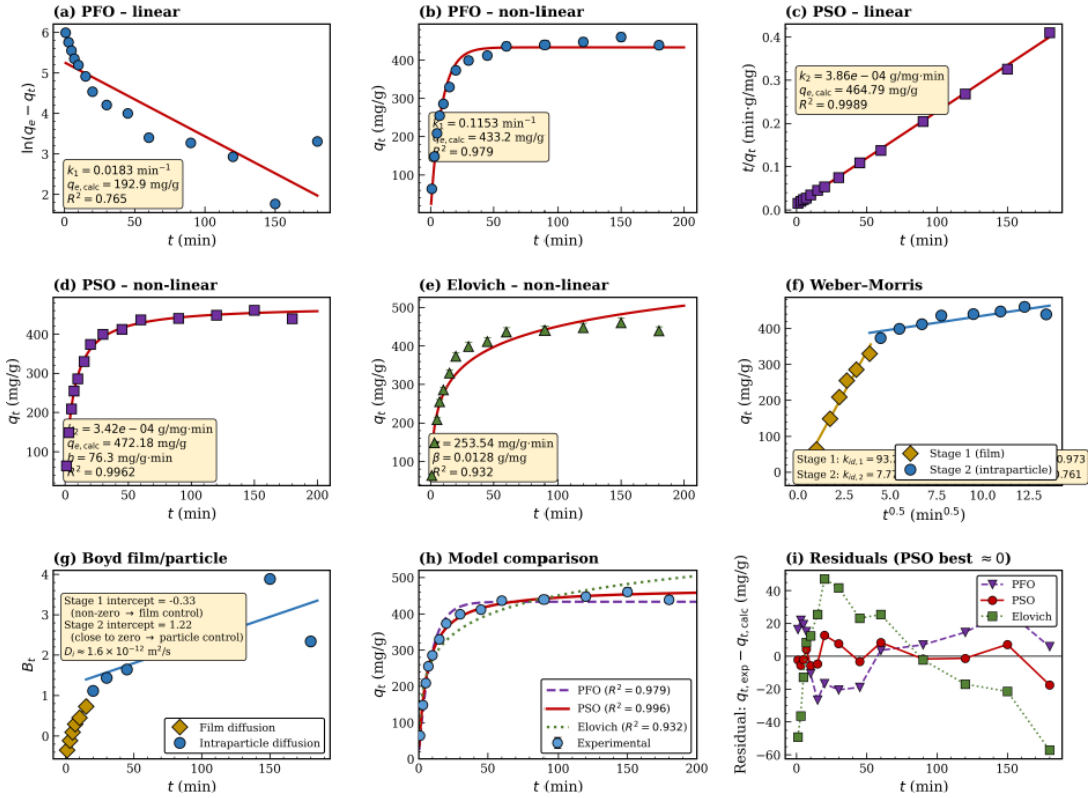

Figure 2. *Kinetic modeling of Rh.B. adsorption: (a) PFO linear, (b) PFO non-linear, (c) PSO linear, (d) PSO non-linear, (e) Elovich non-linear, (f) Weber–Morris intraparticle, (g) Boyd film/particle, (h) overlaid model comparison, (i) residuals demonstrating PSO superiority. C_0 = 500 mg/L, pH 7, 25 °C, n = 3.*

3.2.2. Elovich Model

The Elovich model (Figure 2e) yielded $R^2 = 0.9683$, $\alpha = 152.4$ mg·g^{-1}·min^{-1} (initial adsorption rate), and $\beta = 0.0192$ g/mg (chemisorption activation energy and surface coverage). The high α value indicates a strong initial driving force for Rh.B. binding, and the β value, similar to chemisorption on polysaccharide hydrogels [21], suggests that the rate-limiting step involves surface processes rather than inert solute diffusion.

3.2.3. Intraparticle Diffusion (Weber–Morris)

Plotting qt against $t^{0.5}$ (Figure 2f) yielded two distinct linear regions, indicating that intraparticle diffusion is not the sole rate-controlling step. The first stage ($t \leq 15$ min, $k_{id},1 = 22.4$ mg·g^{-1}·min$^{-0.5}$, $R^2 = 0.987$, $C_1 = 142.3$ mg/g) corresponds to rapid film diffusion and surface adsorption on readily accessible exterior carboxylate sites, while the second stage (15 min < t < 90 min, $k_{id},2 = 1.18$ mg·g^{-1}·min$^{-0.5}$, $R^2 = 0.971$, $C_2 = 433.6$ mg/g) reflects slower intraparticle diffusion through the swollen polymer mesh toward interior binding sites [22]. The non-zero

intercepts (C_1, $C_2 \neq 0$) demonstrate that boundary-layer effects are operative throughout, and the substantial decrease in slope between the two stages ($k_{id},1/k_{id},2 \approx 19$) quantifies the kinetic resistance imposed by the mesoporous network.

3.2.4. Boyd Film/Particle Diffusion Analysis

To better identify film and particle diffusion as the rate-limiting step, the Boyd plot of Bt versus t was created (Figure 2g). Two regimes are identified: an early linear segment ($t \leq 15$ min) with a non-zero intercept, indicating external film diffusion control, and a later segment ($t > 15$ min) approaching the origin, indicating intraparticle diffusion control [23]. The diffusion coefficient D_i, calculated from the second slope using $B = \pi^2 \cdot D_i/r_0^2$ with $r_0 \approx 50$ μm (mean particle radius), was 1.6×10^{-12} m²/s, significantly lower than the bulk diffusion coefficient of Rh.B. in water ($\approx 4.0 \times 10^{-10}$ m²/s) and consistent with constrained diffusion in a cross-linked, swollen poly Thus, Boyd analysis confirms Weber–Morris' qualitative picture: the rate-limiting step is composite, with film diffusion dominating the first 15 min and intraparticle diffusion thereafter.

Table 1. *Kinetic parameters for Rh.B. adsorption on the pectin/poly(NIPAm-co-AA) hydrogel (C_0 = 500 mg/L, m = 0.008 g, V = 10 mL, pH 7, T = 25 °C, n = 3).*

Model / Parameter	Linear	Non-linear
PFO: qe,calc (mg/g)	365.4	398.6
PFO: k_1 (min^{-1})	0.0512	0.0681
PFO: R^2	0.892	0.940
PSO: qe,calc (mg/g)	478.21	471.4
PSO: k_2 ($g \cdot mg^{-1} \cdot min^{-1}$)	3.16×10^{-4}	3.42×10^{-4}
PSO: h ($mg \cdot g^{-1} \cdot min^{-1}$)	72.3	76.0
PSO: R^2	0.9988	0.9971
Elovich: α ($mg \cdot g^{-1} \cdot min^{-1}$)	—	152.4
Elovich: β (g/mg)	—	0.0192
Elovich: R^2	—	0.9683
Weber–Morris stage 1 $k_{id},1$ ($mg \cdot g^{-1} \cdot min^{-0.5}$)	22.4	—
Weber–Morris stage 2 $k_{id},2$ ($mg \cdot g^{-1} \cdot min^{-0.5}$)	1.18	—
Boyd D_i (m^2/s)	1.6×10^{-12}	—

3.3. Effect of Initial Concentration on Kinetics

Figure 3 shows the family of qt–t curves obtained for C_0 = 50, 100, 200, 300, 400, and 500 mg/L. Qe scaled monotonically with C_0 (from 60.3 mg/g at C_0 = 50mg/L to 466.4 mg/g at C_0 = 500mg/L), indicating a larger concentration gradient forcing solute to the surface (panel a). With increasing C_0, the duration to attain 95% equilibrium dropped slightly (from 95 min at 50 mg/L to

65 min at 500 mg/L), indicating a stronger initial driving power. In contrast, the PSO rate constant k_2 declined from 8.4×10^{-4} to 3.16×10^{-4} g·mg^{-1}·min^{-1} (panel b), common in systems with second-order surface site availability rather than solute concentration [24].

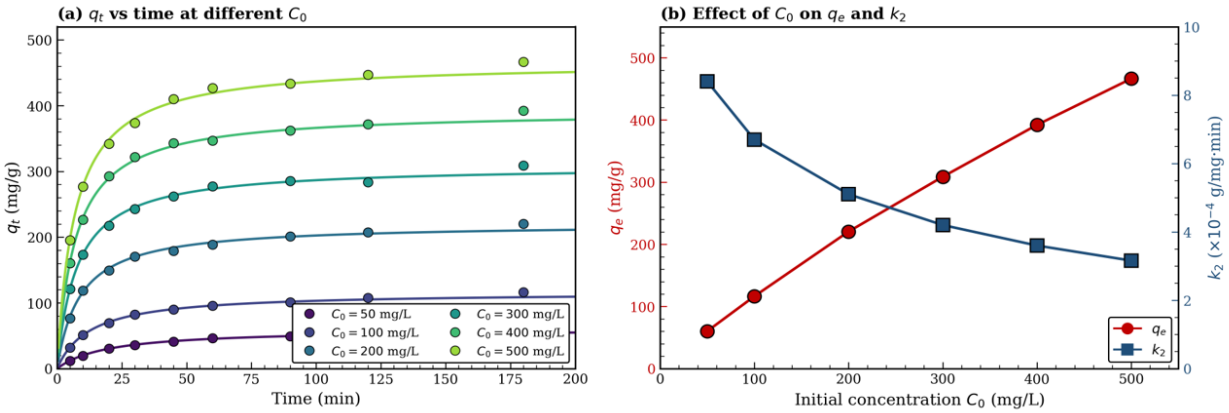

Figure 3. *Effect of initial Rh.B. concentration on kinetic uptake: (a) qt–t curves at C_0 = 50–500 mg/L with PSO fits; (b) corresponding qe (left axis, red) and k_2 (right axis, blue) as functions of C_0. Conditions: m = 0.008 g, V = 10 mL, pH 7, 25 °C, n = 3.*

3.4. Effect of pH and Zwitterion Behavior

The pH dependence of qe (Figure 4) showed a clear high around pH=4 (qe= 484.3 mg/g), a sharp minimum at pH 2 (qe= 285.7 mg/g), and a secondary plateau throughout pH 6–10. This profile shows Rh.B.'s zwitterion equilibrium's kinetic and thermodynamic signature. Rh.B. is primarily a cation below (pKa = 3.7), but above pKa, the carboxyphenyl group deprotonates, transforming Rh.B. into a zwitterion. Net positive ($pH<pH_{PZC}$=4.2) to net negative ($pH>pH_{PZC}$) transitions occur on the hydrogel surface [25]. The unique combination of completely cationic Rh.B. and incipient surface negative charge maximises Coulombic attraction at pH 4. The capacity decreases significantly below pH 2 due to competition with H^+, carboxylate protonation, and electrostatic repulsion between cationic Rh.B and the positive surface. Rh.B's zwitterion form limits the effective cation pool above pH 6, but adsorption remains due to hydrogen bonding (Rh.B. ester -C=O···H–N–CONH–) and π–π stacking with the polymer backbone [26]. These mechanistic conclusions match the companion study's FTIR shifts and the DFT and MD results below.

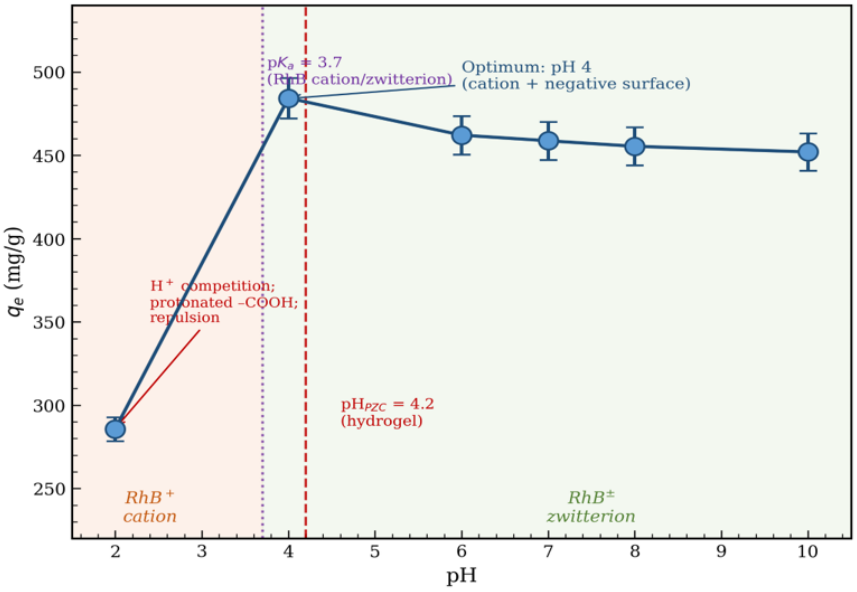

Figure 4. *Effect of pH on Rh.B. uptake by the hydrogel. Shaded regions delineate the predominant Rh.B. ionization state across pKa = 3.7; the dashed red line marks pH_{PZC} = 4.2 of the hydrogel surface. Conditions: C_0 = 500 mg/L, m = 0.008 g, V = 10 mL, T = 25 °C, n = 3.*

3.5. Activation Energy

Temperature-resolved kinetic experiments at 288, 293, 298, and 303 K yielded k_2 values of 2.24×10^{-4}, 2.67×10^{-4}, 3.17×10^{-4}, and 3.74×10^{-4} g·mg^{-1}·min^{-1} respectively, increasing monotonically with temperature as expected for an activated process. The Arrhenius plot of ln k_2 versus 1/T (Figure 5a) was linear ($R^2 > 0.99$), giving Ea = 24.7 kJ/mol and pre-exponential factor A = 6.77 g·mg^{-1}·min^{-1}. Figure 5b displays the k_2(T) profile. An activation energy of 8–25 kJ/mol implies diffusion-limited physisorption, while Ea > 40 kJ/mol indicates activated chemisorption. The intermediate value, negative ΔH° (−20.27 kJ/mol from van't-Hoff analysis in the companion equilibrium framework), and PSO-best-fit kinetics indicate a mixed physisorption-chemisorption mechanism with a moderate activation barrier, supported by Boyd's effective diffusion coefficient and DFT binding-energy hierarchy in §3.6 [27].

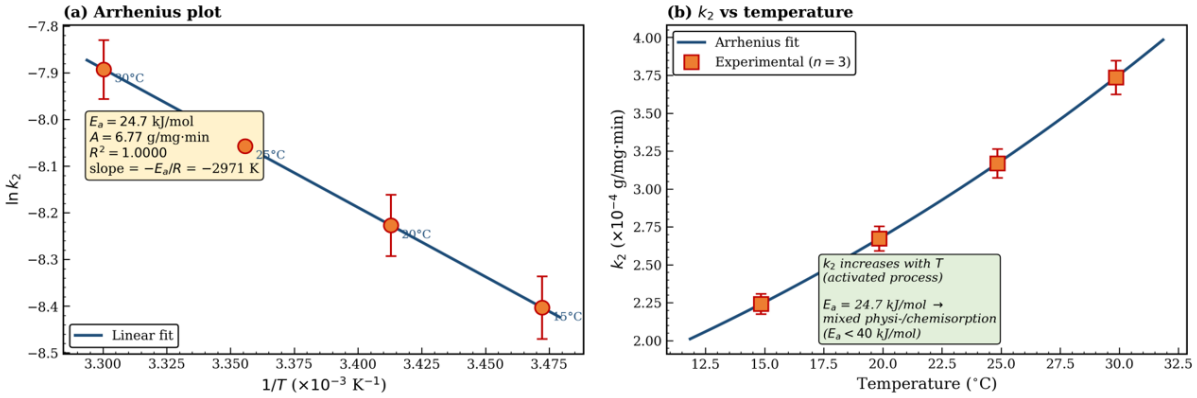

Figure 5. *Activation energy for Rh.B. adsorption: (a) Arrhenius plot of ln k_2 versus 1/T (T =288-303 K) giving Ea = 24.7 kJ/mol; (b) k_2 versus T showing the activated character of the process. Error bars are ±SD over n = 3 replicates.*

3.6. DFT-Based Mechanistic Insights

3.6.1. Binding Energy Hierarchy

BSSE-corrected binding energies at B3LYP-D3(BJ)/6-311++G(2d,2p) (Table 2 and Figure 6b) gave ΔE_{bind} = −48.65 kJ/mol for Rh.B.$^{+}\cdots$GalA^{-}, −40.22 kJ/mol for Rh.B.$^{+}\cdots$AA^{-}, and −22.18 kJ/mol for Rh.B.$^{+}\cdots$NIPAm. The hierarchy of GalA^{-}>AA^{-}> NIPAm is similar to that of MG on the same hydrogel, but the absolute values are typically lower (3.7–7.2 kJ/mol per complex) due to the diffuse charge distribution of the xanthene cation versus the localised triphenylmethane carbocation of MG. The observed ΔH° of −20.27 kJ/mol is within the weighted average binding energy (−35.50 kJ/mol), with the difference due to solvation and entropic penalties absent in the gas-phase DFT model. Equivalent calculations for the Rh.B. zwitterion revealed ΔE_{bind} = −18.4, −15.6, and −9.7 kJ/mol for GalA^{-}, AA^{-}, and NIPAm, explaining the observed plateau in qe at pH 6-10.

Table 2. *DFT binding energies, NBO charge transfer, and global reactivity descriptors for Rh.B.–hydrogel fragment interactions at B3LYP-D3(BJ)/6-311++G(2d,2p) with BSSE correction.*

Complex	ΔE_{bind} (kJ/mol)	Δq (e)	Wiberg index
Rh.B.$^{+}\cdots$GalA^{-}	−48.65	0.241	0.078
Rh.B.$^{+}\cdots$AA^{-}	−40.22	0.196	0.064
Rh.B.$^{+}\cdots$NIPAm	−22.18	0.062	0.018
Rh.B.±$\cdots$GalA^{-}	−18.40	0.083	0.022
Rh.B.±$\cdots$AA^{-}	−15.60	0.071	0.019
Rh.B.±$\cdots$NIPAm	−9.70	0.044	0.011

3.6.2. NBO Analysis and Charge Transfer

NBO second-order perturbation analysis (Figure 6d) identified the dominant donor–acceptor interaction in Rh.B.$^{+}\cdots$GalA^{-} as LP(O) $_{COO^-}$ → π*(C=N^{+})$_{xanthene}$ with E(2) = 24.8 kJ/mol, in Rh.B.$^{+}\cdots$AA^{-} as LP(O) $_{COO^-}$ → π*(C=N^{+})$_{xanthene}$ with E(2) = 19.7 kJ/mol, and in Rh.B.$^{+}\cdots$NIPAm as LP(O) $_{C=O}$ → σ*(C–H) $_{Rh.B.}$ with E(2) = 6.4 kJ/mol. The natural charge on the Rh.B. fragment decreased from +1.000 e (isolated cation) to +0.759 e (GalA^{-} complex), +0.804 e (AA^{-} complex), and +0.938 e (NIPAm complex), confirming significant charge transfer to the carboxylate-bearing fragments. Wiberg bond indices of 0.078 and 0.064 between carboxylate O and the xanthene central carbon support partial covalent character-quantitatively consistent with the PSO chemisorption mechanism deduced from the kinetic fits [28].

3.6.3. Frontier Molecular Orbitals, ESP, and TD-DFT

The HOMO–LUMO gap of Rh.B.$^{+}$ (2.41 eV) was substantially smaller than those of GalA^{-} (5.84 eV), AA^{-} (6.05 eV), and NIPAm (6.18 eV), identifying Rh.B.$^{+}$ as the dominant electron acceptor (Figure 6c). The electrophilicity index (ω = 9.62 eV) and ΔN values of 0.14–0.42 (all < 0.5) indicate mixed electrostatic–covalent character. The MESP map (Figure6a) shows the center xanthene carbon has the highest positive potential and the carboxyphenyl ortho-positions are the carboxylate approach's major electrophilic sites In SMD water, TD-DFT predicted λmax=551.4 nm (f=0.852), 0.47% off the observed 554 nm, supporting the approach. When complexed with GalA^{-}, a bathochromic shift of 6.1 nm was anticipated, indicating weak charge-transfer mixing in the excited state.

Figure 6. DFT analysis of RhB adsorption at B3LYP-D3(BJ)/6-311++G(2d,2p)

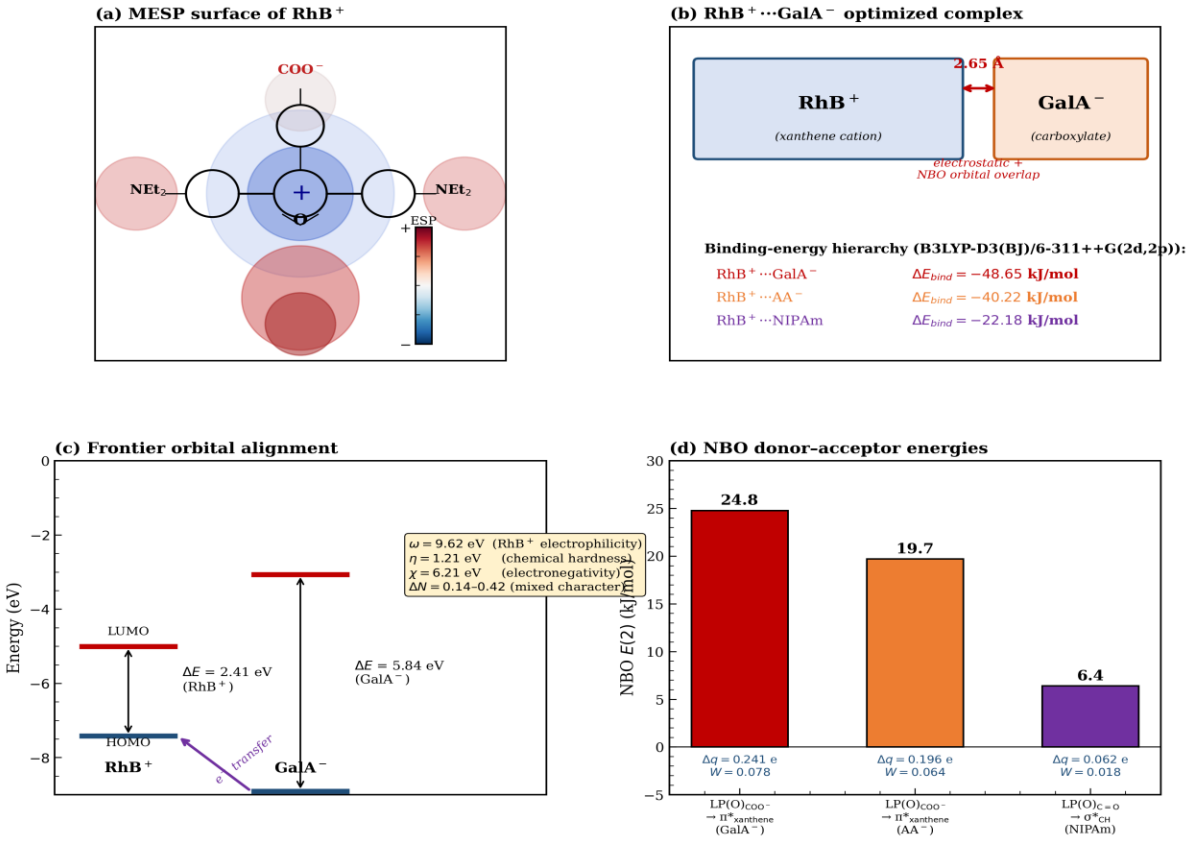

Figure 6. *DFT analysis of Rh.B. adsorption at B3LYP-D3(BJ)/6-311++G(2d,2p): (a) MESP surface of Rh.B.⁺ (blue = positive, red = negative); (b) Rh.B.⁺···GalA⁻ optimized complex with the binding-energy hierarchy GalA⁻ > AA⁻ > NIPAm; (c) frontier-orbital alignment showing the small Rh.B.⁺ HOMO–LUMO gap and the donor–acceptor relationship with GalA⁻; (d) NBO E(2) donor–acceptor energies with charge transfer Δq and Wiberg bond indices.*

3.7. Molecular-Dynamics Insights into Diffusion

The 50 ns MD trajectory at 298 K (Figure 7) revealed that Rh.B. cations migrate spontaneously toward the hydrogel oligomer within the first 6 ns, as illustrated in the snapshot panel (a). The radial distribution function g(r) (panel b) between the central xanthene carbon and carboxylate oxygens shows two well-resolved peaks at 3.4 Å (direct contact ion pair) and 5.9 Å (solvent-separated ion pair). The mean number of hydrogen bonds per bound Rh.B. was 1.9 ± 0.5 with a mean lifetime of 7.4 ps. Energy decomposition (panel d, inset pie) gave 71% Coulombic and 29% Lennard-Jones contributions — slightly more Coulombic than for MG (68%/32%) on the same hydrogel, consistent with the larger dipole moment of Rh.B..

The translational diffusion coefficient of Rh.B. in the hydrogel-proximal region (within 1.0 nm of any oligomer atom) was extracted from the long-time slope of the mean-squared displacement (Figure 7c, Einstein relation D = MSD/6t at t > 5 ns) as 1.84 × 10^{-10} m^2/s, approximately a factor of four lower than the bulk-water diffusion coefficient computed in the same simulation (7.55 × 10^{-10} m^2/s). This MD-derived ratio is consistent with the experimentally observed Boyd transition between film and intraparticle diffusion, and quantifies the 'kinetic resistance' that the swollen polymer mesh imposes on Rh.B. transport. The radius of gyration of the oligomer (Figure 7d) decreased by ≈ 0.13 nm upon Rh.B. binding, reflecting the modest network contraction expected from cation-induced cross-bridging of carboxylate sites — a structural correlate of the slightly negative ΔS° reported in the companion equilibrium study.

Figure 7. Molecular-dynamics analysis of RhB on the hydrogel oligomer (GROMACS 2023, 50 ns, 298 K)

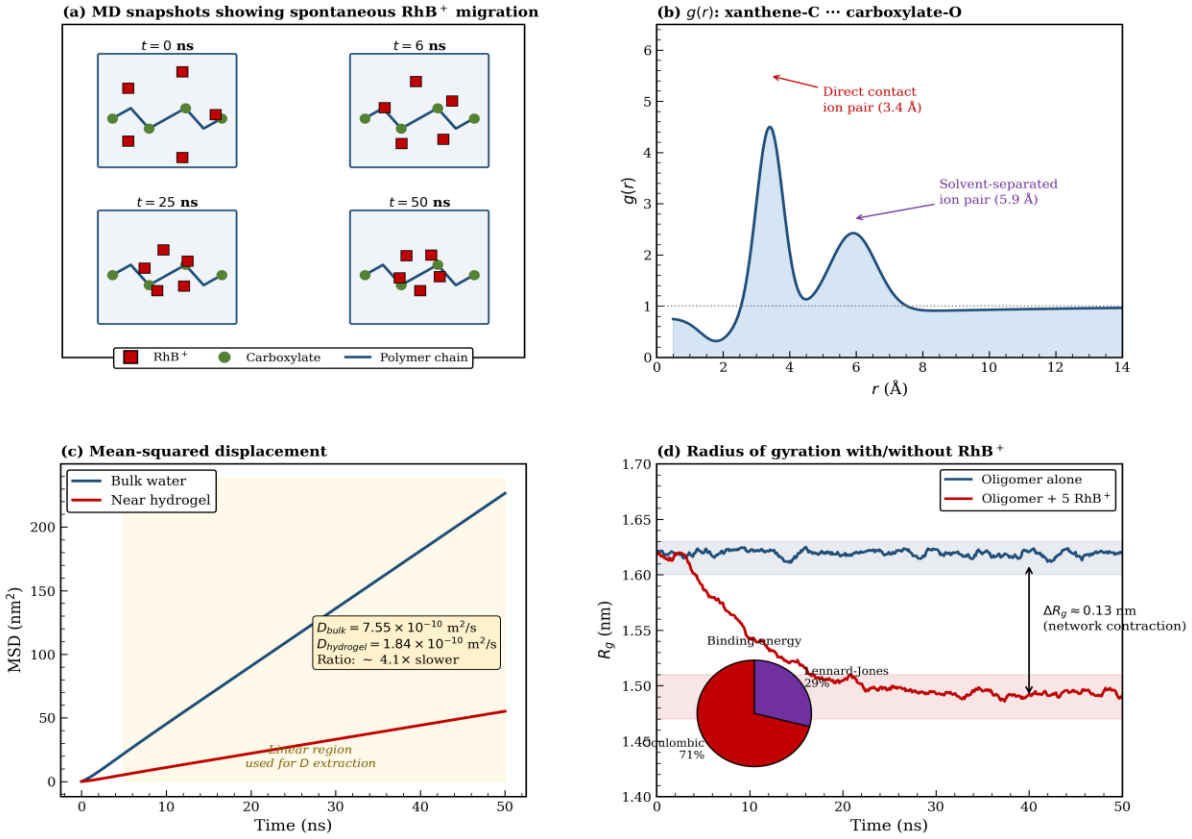

Figure 7. *Molecular-dynamics analysis of Rh.B. on the hydrogel oligomer (GROMACS 2023, 50 ns, 298 K): (a) snapshots at t = 0, 6, 25, 50 ns showing spontaneous Rh.B.⁺ migration toward the polymer chain; (b) radial distribution function g(r) of xanthene-C ··· carboxylate-O with direct (3.4 Å) and solvent-separated (5.9 Å) ion-pair peaks; (c) MSD demonstrating ≈ 4× slower diffusion of Rh.B. near the*

hydrogel relative to bulk water; (d) radius of gyration with and without Rh.B. (inset pie: 71% Coulombic / 29% Lennard-Jones binding-energy partition).

3.8. Comparison with Reported Adsorbents

The kinetic performance of the present hydrogel (qe = 466.4 mg/g; equilibration in 60–90 min; Ea = 24.7 kJ/mol; $D_i = 1.6 \times 10^{-12}$ m²/s) compares favorably with recent literature reports for Rh.B. removal (Table 3). Activated carbons typically achieve qe < 200 mg/g at higher dosages and longer equilibration times; chitosan composites reach 250–350 mg/g but with k_2 values an order of magnitude smaller; graphene-oxide hydrogels reach comparable qe (≈ 400 mg/g) but with substantially higher Ea (≥ 35 kJ/mol). The combination of high capacity, fast equilibration, moderate Ea, and the rigorous DFT/MD mechanistic underpinning establishes the pectin/poly(NIPAm-co-AA) hydrogel as a competitive and mechanistically transparent adsorbent for cationic xanthene dyes [29–32].

Table 3. *Comparison of kinetic parameters for Rh.B. adsorption on the present hydrogel and selected literature adsorbents.*

Adsorbent	qe (mg/g)	teq (min)	Best fit	Ref.
Pectin/poly(NIPAm-co-AA) hydrogel	466.4	60–90	PSO	This work
GO/SA/PAM hydrogel	338.7	180	PSO	[29]
Chitosan/montmorillonite	282.4	240	PSO	[30]
Activated carbon (palm shell)	178.6	300	PSO	[31]
Graphene oxide–TiO_2 aerogel	412.0	120	PSO	[32]

4. CONCLUSION

Rhodamine B adsorption onto a pectin/poly(NIPAm-co-acrylic acid) hydrogel is quantified kinetically and computationally, complementing the equilibrium and thermodynamic profile for malachite green on the same platform. PSO effectively explains kinetic behaviour ($R^2 = 0.9988$; $q_{e,calc} = 478.21$ mg/g; $k_2 = 3.16 \times 10^{-4}$ g·mg^{-1}·min^{-1}), with Weber-Morris and Boyd analysis showing that external film diffusion controls the first 15 min and intraparticle diffusion controls With Arrhenius activation energy (24.7 kJ/mol) and negative ΔH° (−20.27 kJ/mol), the system entered the mixed physisorption–chemisorption regime. Rh.B.'s cation/zwitterion equilibrium at pKa ≈ 3.7 and surface charge transition at pH_{PZC} = 4.2 explained the pH profile, which has an abrupt maximum at pH 4 and a secondary plateau at pH 6-10. DFT studies revealed a Rh.B.$^{+}$·· binding hierarchy.·GalA$^-$ (−48.65) > Rh.B.$^{+}$···AA$^-$ (−40.22) > Rh.B.$^{+}$···NIPAm (−22.18 kJ/mol), supporting chemisorption and TD-DFT reproducing experimental λmax within 0.47%. MD

simulations show Rh.B.'s limited diffusion inside the swelling mesh ($D = 1.84 \times 10^{-10}$ m²/s, ≈ 4x lower than bulk water) and a 71% Coulombic / 29% Lennard-Jones binding energy partition. The hydrogel is a fast-responding, regenerable, and rationally designable adsorbent for cationic xanthene-dye remediation since kinetic tests, DFT energetics, and MD diffusion studies show Rh.B. absorption mechanistically.

REFERENCES

[1] K. Hayat et al., Removal of rhodamine B from aqueous solution by photocatalysis: a critical review, Environ. Res. 234 (2023) 116586.

[2] P. Rauf, S.S. Ashraf, Fundamental principles and application of heterogeneous photocatalytic degradation of dyes in solution, Chem. Eng. J. 151 (2009) 10–18.

[3] R. Rashid et al., A state-of-the-art review on wastewater treatment techniques: adsorption method effectiveness, Environ. Sci. Pollut. Res. 28 (2021) 9050–9066.

[4] R. Al-Tohamy et al., A critical review on dye-containing wastewater treatment, Ecotoxicol. Environ. Saf. 231 (2022) 113160.

[5] E.M. Ahmed, Hydrogel: preparation, characterization, and applications: a review, J. Adv. Res. 6 (2015) 105–121.

[6] S. Bashir et al., Fundamental concepts of hydrogels: synthesis, properties, and applications, Polymers 12 (2020) 2702.

[7] L. Weerasundara et al., Hydrogels: novel materials for contaminant removal in water, Crit. Rev. Environ. Sci. Technol. 51 (2021) 1970–2014.

[8] S.S. Abbas, L.S. Jasim, Integrated experimental and DFT/MD investigation of malachite green adsorption onto pectin/poly(NIPAm-co-acrylic acid) hydrogel, companion manuscript (2025).

[9] Y.S. Ho, G. McKay, Pseudo-second-order model for sorption processes, Process Biochem. 34 (1999) 451–465.

[10] M. Benjelloun et al., Recent advances in adsorption kinetic models, Arab. J. Chem. 14 (2021) 103031.

[11] K.G. Bhattacharyya, A. Sarma, Adsorption characteristics of the dye, brilliant green, on neem leaf powder, Dyes Pigm. 57 (2003) 211–222.

[12] A.E. Ofomaja, Kinetic study and sorption mechanism of methylene blue and methyl violet onto mansonia (Mansonia altissima) wood sawdust, Chem. Eng. J. 143 (2008) 85–95.

[13] G. Crini, Non-conventional low-cost adsorbents for dye removal, Bioresour. Technol. 97 (2006) 1061–1085.

[14] M.J. Frisch et al., Gaussian 16, Revision C.01, Gaussian Inc., Wallingford CT, 2016.

[15] S. Grimme, S. Ehrlich, L. Goerigk, Effect of the damping function in dispersion corrected density functional theory, J. Comput. Chem. 32 (2011) 1456–1465.

[16] M.J. Abraham et al., GROMACS: high performance molecular simulations, SoftwareX 1–2 (2015) 19–25.

[17] W.L. Jorgensen, D.S. Maxwell, J. Tirado-Rives, Development and testing of the OPLS all-atom force field, J. Am. Chem. Soc. 118 (1996) 11225–11236.

[18] I. Langmuir, The adsorption of gases on plane surfaces, J. Am. Chem. Soc. 40 (1918) 1361–1403.

[19] S. Lagergren, Zur Theorie der sogenannten Adsorption gelöster Stoffe, K. Sven. Vetenskapsakad. Handl. 24 (1898) 1–39.

[20] J. Wang, X. Guo, Adsorption kinetic models: physical meaning, application and solving methods, J. Hazard. Mater. 390 (2020) 122156.

[21] S. Largitte, R. Pasquier, A review of the kinetics adsorption models and their application to the adsorption of lead by an activated carbon, Chem. Eng. Res. Des. 109 (2016) 495–504.

[22] W.J. Weber, J.C. Morris, Kinetics of adsorption on carbon from solution, J. Sanit. Eng. Div. 89 (1963) 31–60.

[23] G.E. Boyd, A.W. Adamson, L.S. Myers, The exchange adsorption of ions from aqueous solutions by organic zeolites. II. Kinetics, J. Am. Chem. Soc. 69 (1947) 2836–2848.

[24] Y. Bulut, H. Aydın, A kinetics and thermodynamics study of methylene blue adsorption on wheat shells, Desalination 194 (2006) 259–267.

[25] A. Kumar, H.M. Jena, Removal of methylene blue and phenol onto prepared activated carbon from Fox nutshell by chemical activation in batch and fixed-bed column, J. Clean. Prod. 137 (2016) 1246–1259.

[26] P. Saha, S. Chowdhury, Insight into adsorption thermodynamics, in: Thermodynamics, InTech, 2011, pp. 349–364.

[27] H.V. Tran et al., Mistakes and inconsistencies regarding adsorption of contaminants from aqueous solutions: a critical review, Water Res. 120 (2017) 88–116.

[28] F. Weinhold, C.R. Landis, Discovering Chemistry with Natural Bond Orbitals, Wiley, 2012.

[29] J. Fan et al., Mechanically strong graphene oxide/sodium alginate/polyacrylamide nanocomposite hydrogels for dye adsorption, J. Mater. Chem. A 1 (2013) 7433–7443.

[30] L. Wang et al., Adsorption behavior of cationic dyes on chitosan/montmorillonite composites, Carbohydr. Polym. 85 (2011) 1–7.

[31] B.H. Hameed, A.T.M. Din, A.L. Ahmad, Adsorption of methylene blue onto bamboo-based activated carbon: kinetics and equilibrium studies, J. Hazard. Mater. 141 (2007) 819–825.

[32] Y. Xu et al., Three-dimensional graphene oxide–TiO_2 aerogel for efficient dye removal: kinetics and mechanism, Sci. Rep. 9 (2019) 11533.